



# A point field driven approach to process metrics based on laser powder bed fusion additive manufacturing models and in situ process monitoring

Samuel J. A. Hocker<sup>1,a)</sup> , Brodan Richter<sup>1</sup>, Peter W. Spaeth<sup>1</sup>, Andrew R. Kitahara<sup>2</sup>, Joseph N. Zalameda<sup>1</sup>, Edward H. Glaessgen<sup>1</sup>

<sup>1</sup>NASA Langley Research Center, Hampton, VA, USA

<sup>2</sup>National Institute of Aerospace, Hampton, VA, USA

<sup>a)</sup>Address all correspondence to this author. e-mail: samuel.hocker@nasa.gov

Received: 24 October 2022; accepted: 9 February 2023; published online: 16 March 2023

The widespread adoption of additive manufacturing (AM) in different industries has accelerated the need for quality control of these AM parts. Some of the complex and labor-intensive challenges associated with qualification and certification of AM parts are addressed by modeling and monitoring process conditions. Quantifying melt-track process conditions remains a significant computational challenge due to the large-scale differential between melt pool and part volumes. This work explores a novel point field (PF) driven AM model-based process metric (AM-PM) approach for calculating melt track resolved process conditions with maximal computational speed. A cylindrical Ti-6Al-4V test article with 16 equiangular zones having varied process parameters was built. The melt-track resolved AM-PMs were calculated and mapped to porosity existence for the 5.8-million-point PF of the test article. AM-PMs were calculated in 6.5 min,  $\sim 665\times$  faster than a similarly sized finite element calculation. This approach enables efficient prediction, assessment, and adjustment of AM builds.

## Introduction

AM is a technology that is shifting both design and manufacturing paradigms [1–3]. The AM process involves building parts iteratively, step-by-step and layer-by-layer [3–5]. The precise sequence allows for the creation of parts with complex geometrical features that would be difficult, and often impossible to fabricate otherwise. AM has been employed in the design of structural parts with maximized strength-to-weight ratios and propulsion components with integrated cooling systems [6]. The ability of AM to produce near-net-shape parts reduces material wastage and manufacturing costs [3, 7–9]. However, defect formation during the AM process can compromise part performance [10]. The qualification practices for AM parts is an active area and the standards are being developed and modified [2, 3, 5, 11]. The rationale for qualified AM parts will depend on the industry and end application, but it is expected to be based on four governing principles: qualified material process, statistical process control, materials properties suite, and a qualified part process [3]. To enable AM and its advantages to contribute to aerospace and other high-performance applications, it is critical

to develop capabilities for statistical process control by understanding, simulating, and preventing defect formations during the AM process [2, 3]. In particular, part to part build quality must be robust in order to qualify AM parts for any application [1, 2].

Laser powder bed fusion (L-PBF) is a specific type of AM that uses a powder feedstock that is spread upon a flat substrate and fused by a laser heat source [3–5]. The fusion process requires both the feedstock and the immediately adjacent substrate to melt [12–14]. The short duration, translating melt created by the scanning laser is referred to as a melt pool [15–19]. Melt pool control governs the quality of the weld and, thus, the quality of the part created by the L-PBF AM process.

Defect formation during the build process is usually undesirable and detrimental to the quality of an AM part [10, 20, 21]. A common defect that occurs during L-PBF AM is the formation of porosity induced by keyhole or lack of fusion mechanisms. Porosity is a complex phenomenon that arises from interactions between the feedstock and the process dynamics. The formation strongly depends on the liquation, vaporization,

and solidification sequence [14, 22–25]. Understanding the causalities of porosity is critical to the qualification of AM parts [11]. Part-scale AM builds must be assessed for the melt track resolved risks of porosity occurrence, both when planning and reviewing a part for aerospace qualification [1, 2, 11].

The L-PBF AM process is the result of a build strategy applied to parts oriented in the build envelope [3–5]. A build strategy is comprised of laser powers, foci, and velocities orchestrated in hatch patterns and spacings such that the fusion of feedstock is overlapped to consolidate fully dense additively manufactured parts [12]. When general build strategies are applied to a part, unexpected process conditions can result in underheating or overheating that lead to inconsistent fusion [26]. Hatch pattern, laser power, velocity, and layer thickness are among the primary settings that comprise a build strategy. Each build strategy decision contributes to the overall build quality. AM process design engineers typically develop generalized build strategies that rely on heuristic rules and guidelines to design successful builds [1, 3, 27]. The need for generalized build strategies is due to the broad time and length scales associated with the L-PBF process compared to the melt events [3, 7, 27].

The complex challenge of qualification and certification of high quality AM parts can be informed by using computationally efficient multi-scale AM models [2, 27, 28]. Several AM modeling approaches have been developed to predict the temperature field and temperature history of the L-PBF AM process. While valuable for understanding the AM process, high-fidelity melt pool models [15, 29, 30] do not significantly inform certification and qualification of parts due to their limited simulation scales and high computational cost [28]. Analytical AM models are computationally efficient approaches that include melt pool models [16, 31–36], layer-by-layer thermal models [37–43], and velocity-power process maps [14, 17, 22, 44]. Among these, the graph theory-based models [37–43] and neighboring effect AM modeling method [36] are PF driven methods. The graph theory-based models [37–43] calculate a layer-by-layer thermal history using successive time steps. The neighboring effect AM modeling method [36] predicts melt pool areas via neighborhood effected power-velocity and energy density models; and requires experimental data to identify optimal coefficients. The variety of these AM modeling approaches reflects the computational challenge associated with the very large-scale differentials between melt pools and part volumes in L-PBF AM.

The scale differentials of the L-PBF AM process can be considered in terms of the melt pool and part volumes. There is a huge differential between the melt pool volume, estimated at  $2\text{E}-11\text{ m}^3$ , and the overall part volume, from  $1\text{E}-9\text{ m}^3$  to  $6.4\text{E}-2\text{ m}^3$  [1]. The differential translates to 0.05 to 3.2 trillion melt pools per part, and more if melt pool overlaps are considered. This very large range of scale for L-PBF AM parts remains a significant computational challenge due to modeling and hardware limitations

for characterizing and predicting the melt track resolved process conditions.

The objective of this work is to develop the most computationally efficient approach to assess the AM process at the part scale using AM models. The PF driven process metric (PM) approach to AM modeling addresses the need for a methodology to compute the expected and observed melt track resolved process conditions throughout the AM build process. The AM-PM approach is a PF driven non-constant kernel convolution calculation. The method comprises a point-wise analytical AM model defined kernel function and a neighborhood search algorithm to calculate measures of the physical state at each point in a PF. The PMs are instantaneous point-in-time data that can be used for part-scale assessment of the AM build integrity or design improvements. The AM-PM approach displays a novel combination of computational speed and precision when compared with other AM modeling approaches. AM-PM allows for multiple analytical AM models to be calculated directly from a PF in a single pass and requires only material property inputs. As a result, AM-PM calculations have a maximal computational speed for quantifying melt track resolved process conditions from the PF data. AM-PM calculations enable efficient prediction, assessment, and adjustment of AM builds for reducing defects and developing statistical process controls.

## The AM-PM approach

### Point field

An AM PF is a collection of points having time resolved spatial coordinates and any additional information required to describe an AM build, such as the laser spot size and power for L-PBF AM. A model PF can be generated from a build file. Alternatively, a measured PF can be obtained from in-situ sensors that record the time resolved mirror positions and laser powers for L-PBF. The PF is evaluated in terms of a principal point,  $i$ , and its neighbors,  $j$ , Fig. 1. The time resolved sequence of the PF points defines the laser spot (heat source) movements, while the laser power levels define whether the movement is a hatch, power on, or a jump, power off. The angles of neighboring meandering hatches have a difference of  $\pi$  radians, Fig. 1.

### Process metric

The PM calculation is the convolution of a non-constant kernel function,  $f_{ij}$ , with the neighborhood of the principal point,  $\varnothing_{ij}$ , Eq. 1. A  $PM_i$  is the calculated PM value at each principal point  $i$ . The chosen kernel function and neighborhood search algorithm are defined by the physical model of the AM process that is being considered for each principal point in the PF.

$$PM_i = \sum_j^N f_{ij} \varnothing_{ij}. \quad (1)$$

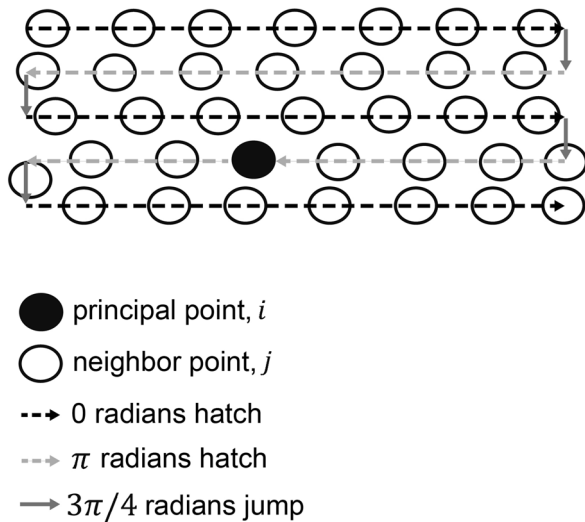


**Figure 1:** Schematic of PF principal and neighbor points of an AM process, with the hatch angles and jump movements indicated.

### Search algorithm

The neighborhood is determined for each principal point by a search algorithm, or function set,  $\emptyset_{ij}$ . In this work, a Heaviside function was used such that 1 was returned when the spatial and temporal conditions were satisfied and 0 otherwise, Eq. 2. The neighborhood search algorithm may include spatial conditions such that the distance,  $r_{ij}$ , is less than or equal to a variable neighborhood distance,  $R_i$ .

$$\emptyset_{ij} = \begin{cases} 1 & \text{if } r_{ij} \leq R_i \ \& \ \tau_{ij} \geq t_i^{delay} \\ 0 & \text{else} \end{cases} \quad (2)$$

The distance,  $r_{ij}$ , between the principal  $i$  and the neighborhood point  $j$  is calculated using the three-dimensional (3D) cartesian coordinate distance,

Equation 3. By setting  $R_i$  to a constant value  $C$ , Eq. 4, a non-variable PM neighborhood distance,  $R_i^C$ , can be taken as a neighborhood radius. The coordinate distances on the x, y and z axes are calculated between the principal point  $i$  and the neighborhood point  $j$ , Eq. 5–7.

$$r_{ij} = \sqrt{dx_{ij}^2 + dy_{ij}^2 + dz_{ij}^2}, \quad (3)$$

$$R_i^C = C, \quad (4)$$

$$dx_{ij} = x_i - x_j, \quad (5)$$

$$dy_{ij} = y_i - y_j, \quad (6)$$

$$dz_{ij} = z_i - z_j. \quad (7)$$

For the AM-PM approach, time is recorded in the PF with a resolution that is equal or better than the characteristic timescale of the process, 10  $\mu$ s for digital galvanometers used in L-PBF AM

instruments. The time component of the neighborhood search algorithm is defined as the difference in time,  $\tau_{ij}$ , being greater than or equal to a variable time delay,  $t_i^{delay}$ . Relative to the principal point, the neighborhood may be composed of points in the past,  $\tau_{ij}^P$ , Eq. 8; future,  $\tau_{ij}^F$ , Eq. 9; or both,  $\tau_{ij}^A$ , Eq. 10.

$$\tau_{ij}^P = t_i - t_j, \quad (8)$$

$$\tau_{ij}^F = t_j - t_i, \quad (9)$$

$$\tau_{ij}^A = abs(t_i - t_j). \quad (10)$$

### Kernel functions

#### Melt pool dimension Kernel functions

In L-PBF AM, the patterned movement of the laser across the feedstock creates a melt pool to fuse the powder to the substrate. The melt pool dimensions can be estimated from the material properties and process parameters. As PMs, the melt pool depth,  $D_i$ , and width,  $W_i$ , can be calculated for each principal point, Eq. 11 and Eq. 12 [16]. Here,  $A$  is the absorptivity;  $P$  is the wattage of the incident heat source;  $\rho$  is the bulk material density;  $c_p$  is the bulk material specific heat capacity;  $V_{ij}$  is the velocity of the melt pool;  $T_m$  is the melting temperature of the material;  $T_0$  is the substrate temperature; and  $e$  is Euler's number.

$$D_i = \sqrt{\frac{2AP_i}{e\pi\rho c_p(T_m - T_0)V_{ij}}}, \quad (11)$$

$$W_i = 2D_i. \quad (12)$$

#### Velocity Kernel function

The L-PBF AM process model of the melt pool velocity was taken to be equivalent to the velocity of the laser spot. The neighborhood search algorithm for the melt pool velocity PM was  $j$  equal to  $i - 1$  and the kernel function was  $r_{ij}$  over  $\tau_{ij}^P$ , Eq. 13.

$$V_{ij} = \frac{r_{ij}}{\tau_{ij}^P}. \quad (13)$$

#### Lack of fusion Kernel function

Tang et al. [12] presented an AM process model showing that lack of fusion porosity happens when the melt pool shape is too small to overlap for a given hatch spacing and layer height. The lack of fusion model from Tang et al. [12] can be calculated as a PM, or criterion, for each principal point once the hatch spacing and layer heights are known at each point. The hatch spacing metric requires a distance measurement to be taken between the principal point and its nearest neighbor within the parallel adjacent melt track. To calculate the hatch spacing at each principal point, a neighborhood search algorithm must be used such that the neighborhood consists of only the nearest neighbor within the parallel adjacent

melt track. The neighborhood search algorithm was such that  $3\pi/2 > \text{abs}(\theta_i^H - \theta_j^H) > \pi/2$  and  $r_{ij} < r_{ik}$ , where  $k$  is  $j - 1$ . The absolute value of the hatch angle difference being less than  $3\pi/2$  and greater than  $\pi/2$  ensured that the neighbor point was on a separate melt track of the meander hatch pattern. The angle  $\theta_{ij}$  relative to the x-axis at each principal point was calculated from arctangent of  $dy_{ij}$  over  $dx_{ij}$ , Eq. 14. The angle relative to the x-axis is a phase sensitive hatch angle,  $\theta_i^H$ , when  $\theta_{ij}$  is equal to  $\theta_{ik}$ , where  $k$  is  $i - 1$ , Fig. 1. The equation of distance for a point from a line was the kernel function between the principal point and the neighborhood, Eq. 15. The resulting PF driven PM was the hatch distance at each principal point.

$$\theta_{ij} = \arctan\left(\frac{dy_{ij}}{dx_{ij}}\right), \quad (14)$$

$$f_{ij}^H = |\cos(\theta_i^H)dy_{ij} - \sin(\theta_i^H)dx_{ij}|. \quad (15)$$

The inter layer thickness at the principal point,  $dz_{ij}^H$ , was determined using a search algorithm such that  $dz_{ij}$ , Eq. 7, was a minimum value greater than zero. A threshold value of 1 for  $l_{ij}$  in the lack of fusion criterion AM model indicates that lack of fusion porosity will occur. The  $l_{ij}$  AM-PM can be calculated for each principal point, Eq. 16, once the calculated melt pool dimensions, hatch spacing, and inter-layer thickness are known at each principal point.

$$l_{ij} = \left(\frac{f_{ij}^H}{W_i}\right)^2 + \left(\frac{dz_{ij}^H}{D_i}\right)^2. \quad (16)$$

### Thermal rise Kernel function

A thermal rise is defined as a temperature increase relative to a reference, such as ambient temperature. The AM-PM approach can be used to determine a PF driven thermal rise at each principal point. The discrete heat source AM process model described in Groeber et al. [32] was adapted as a non-constant kernel function where  $\nu$  is the sampling frequency,  $\sigma$  is the radius of the heat source, and  $\alpha$  is the thermal diffusivity of the material, Eq. 17. The thermal rise AM-PM can be interpreted as a transient measure of localized pre-heat temperature when a time delay,  $t_i^{delay}$ , term is utilized and  $\tau_{ij}$  is defined by Eq. 8. A time delay of 157  $\mu$ s was chosen such that the neighborhood search algorithm includes only points that are behind the incident heat source.

$$f_{ij}^G = \frac{AP_j}{\nu_j \rho c_p \sqrt{2\pi} \frac{2}{3} (\sigma_j^2 + 2\alpha \tau_{ij})^{\frac{2}{3}}} \exp\left(\frac{-r_{ij}^2}{2(\sigma_j^2 + 2\alpha \tau_{ij})}\right). \quad (17)$$

## Results

A complex L-PBF AM build was designed to generate a Ti-6Al-4V cylindrical test article that contained 16 equiangular zones, each with different AM parameter combinations, Table 1 and

**TABLE 1:** Build parameters and calculated melt pool widths for each equiangular zone of the specimen.

Equi- angular zone	Power [W]	Velocity [mm/s]	$\theta_i^{2.05r}$ [rad]	Calculated melt pool width [mm]
1	221	1176	0.526	0.117
2	221	1092	0.922	0.121
3	221	1008	1.313	0.126
4	221	924	1.707	0.132
5	221	840	2.100	0.138
6	221	756	2.499	0.146
7	221	672	2.885	0.155
8	221	588	0.138	0.165
9	308	1176	0.143	0.138
10	308	1092	2.887	0.143
11	308	1008	2.494	0.149
12	308	924	2.103	0.156
13	308	840	1.708	0.163
14	308	756	1.317	0.172
15	308	672	0.925	0.183
16	308	588	0.532	0.195

Fig. 2(a). The parameters chosen produced a range of L-PBF AM process conditions that would result in fully consolidated material, equiangular zones dominated by lack of fusion porosity, and those with keyhole porosity. The zone-wise parameters were reduced to a single value of calculated melt pool width, Eq. 12. The calculated melt pool widths ranged from 117 to 195  $\mu$ m and were used to identify the 16 equiangular zones, Fig. 2(a). The porosity was measured using X-ray computed tomography (XCT) and registered to the measured PF, Fig. 2(c) and (d). Both measured and modeled PFs of this challenging test article were used to highlight the computational speed and utility of the AM-PM approach for quantifying correlations of melt track resolved process conditions to porosity.

The 16 equiangular zones were distinguishable in the photographed surface features, Fig. 2(b). Equiangular zones 1–4 appeared to be dominated by darkened surface features indicative of pores. Spatter ejecta, with approximately 200  $\mu$ m diameters, appeared to be welded randomly upon the surface. The melt track resolved thermal rise for equiangular zones 9–16 resulted in a melt feature extending various distances from the center of the test article: 2.7, 3.2, 3.1, 3.1, 3.7, 4.8, 4.4, and 4.2 mm, respectively. The surface features correlating to the different equiangular zone boundaries were also visible in the XCT measurement, Fig. 2(c). The specimen showed increased height at the geometric boundaries of equiangular zones 3–16. In equiangular zones 1–3, the feature heights above the relative surface were approximately 200  $\mu$ m, Fig. 2(c), and pores were evident throughout, Fig. 2(d).

The registration of the XCT measurements to each of the process points provided a per point classification of porosity or

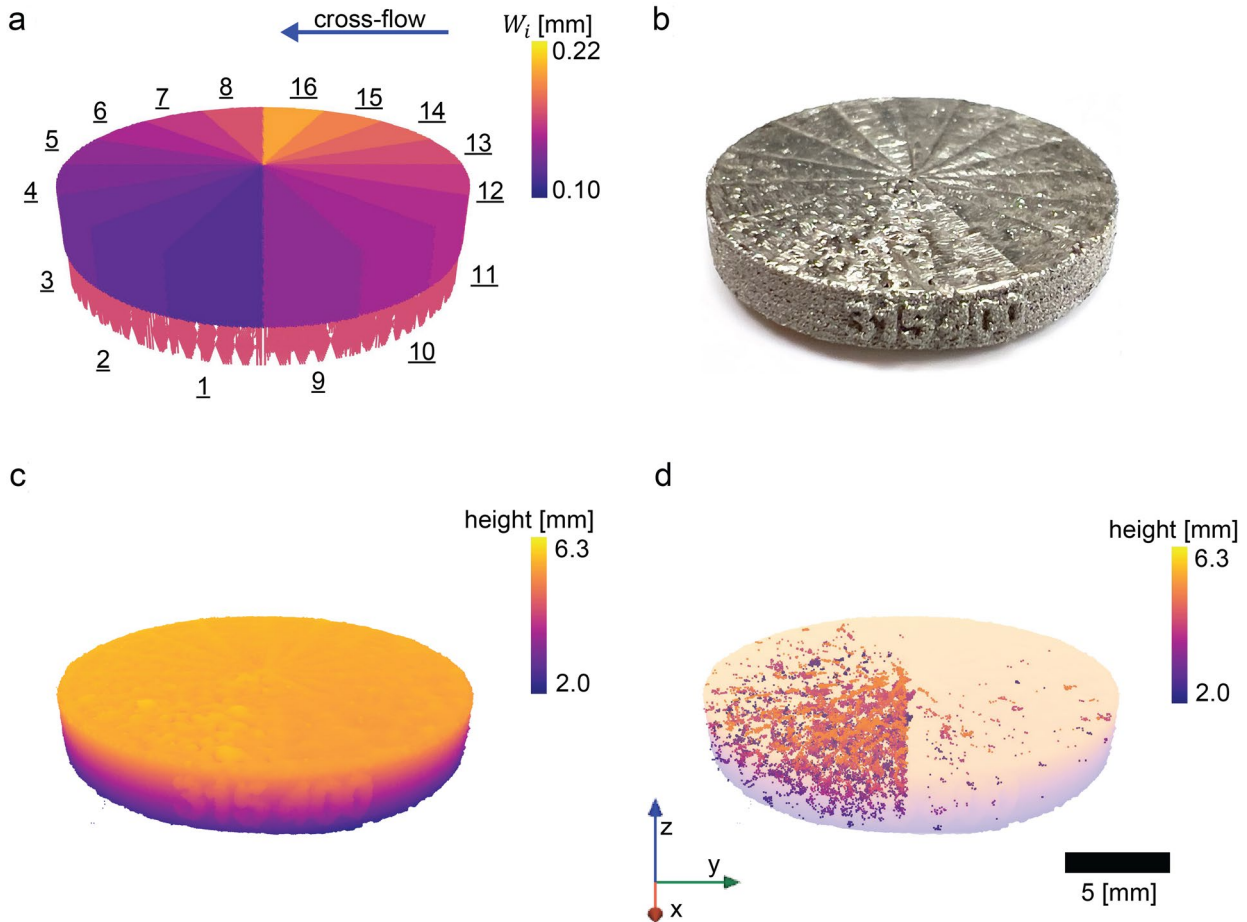


**Figure 2:** An illustrated summary of the test article with the 16 equiangular zones. (a) 3D PF plot of Eq. 12, the calculated width of the melt pool per melt track resolved process conditions. (b) photograph. (c) XCT color mapped to the build height. (d) porosity features color mapped to the build height.

solid, i.e., a material phase field. Equiangular zones 1–3 had the smallest calculated melt pool widths and showed process point porosity populations greater than 1 percent, Fig. 3.

The thermal rise AM-PMs are melt-track resolved heating quantified for the AM build process. The thermal rise PMs were plotted against the calculated melt pool widths as heat maps with bin edges that ranged from 0 to 4000  $\Delta K$  and a step size of 20  $\Delta K$ , and calculated melt pool widths that ranged from 80 to 400  $\mu m$  with a 0.5  $\mu m$  step size, Fig. 4. The bins with greater than 100 counts were considered as the population peak area. The population peak area showed a range of calculated melt pool widths from 113 to 202  $\mu m$  and a thermal rise range was from 45 to 2000  $\Delta K$ , Fig. 4(a). The percent porosity population fraction, Fig. 4(b), showed a range of calculated melt pool widths from 113 to 127  $\mu m$  and the thermal rise range was from 0 to 1000  $\Delta K$ .

The lack of fusion AM-PMs are based on the Tang et al. [12] AM model for lack of fusion prediction and were plotted as a heat map of the subcomponents of Eq. 16, Fig. 5. The heat map

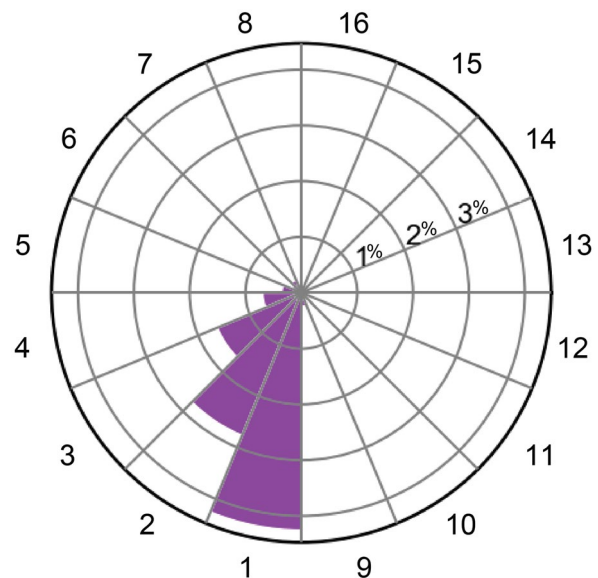


**Figure 3:** Radial histogram of the porosity fraction in percent. The magnitude is shown by expanding concentric rings and aligned with each equiangular zone of the specimen.

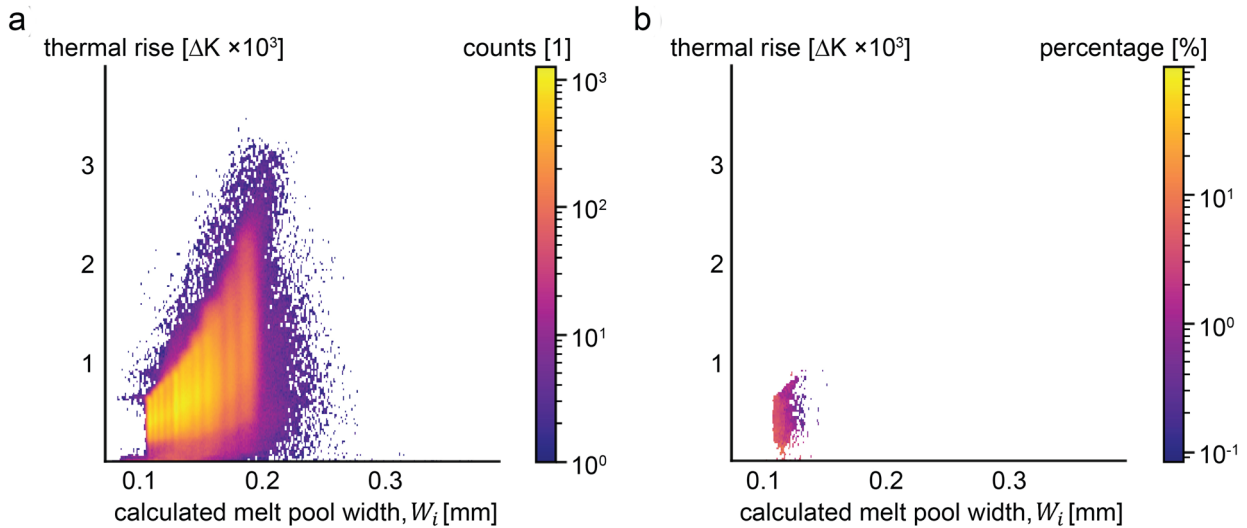


**Figure 4:** Heat map histograms of the thermal rise for (a) the measured PF and (b) percent porosity population fraction plotted against the calculated melt pool widths.

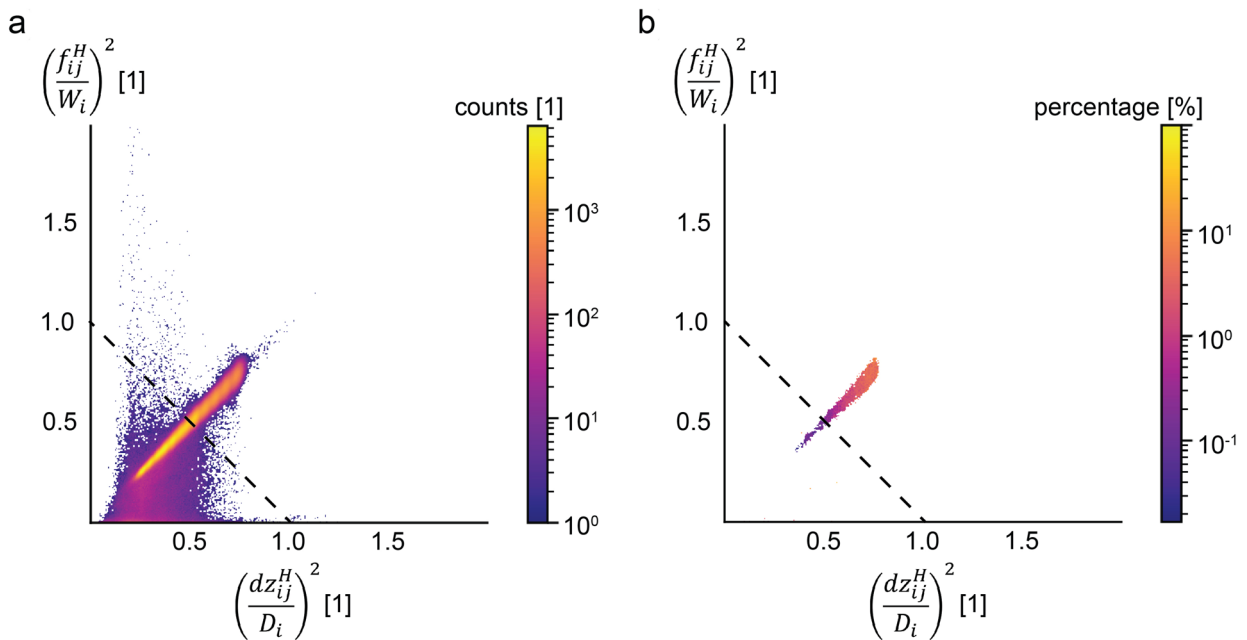


**Figure 5:** Heat map histograms of the lack of fusion model parameters for (a) the measured PF and (b) percent porosity population fraction.

bins ranged from 0 to 2 and had a step size of 0.004. The lack of fusion model threshold value of 1 is marked by a dashed line. The distance from the origin to each bin is the lack of fusion PM. The bins that were greater than 100 counts had lack of fusion values that ranged from 1.6 down to 0.44. The porosity fraction had lack of fusion values that ranged from 1.6 down to 0.8.

The selected PMs of the measured and modeled PFs of the test article were mapped in 3D plots, Fig. 6. The measured PFs consisted of the time resolved laser position and power values

that were recorded by the L-PBF AM instrument during the build process. The PMs, including thermal rise and melt pool width, were calculated using the AM-PM approach as applied to the modeled and measured PF values, respectively. The variations that arose during the process were observed for each of the mapped PMs, Fig. 6(a–e). These variations were most prominent at the equiangular zone boundaries of the test article, most notably in the hatch velocity PMs, Fig. 6(a). The modeled PFs are the ideal behaviors, and notable variations are present for the lack of

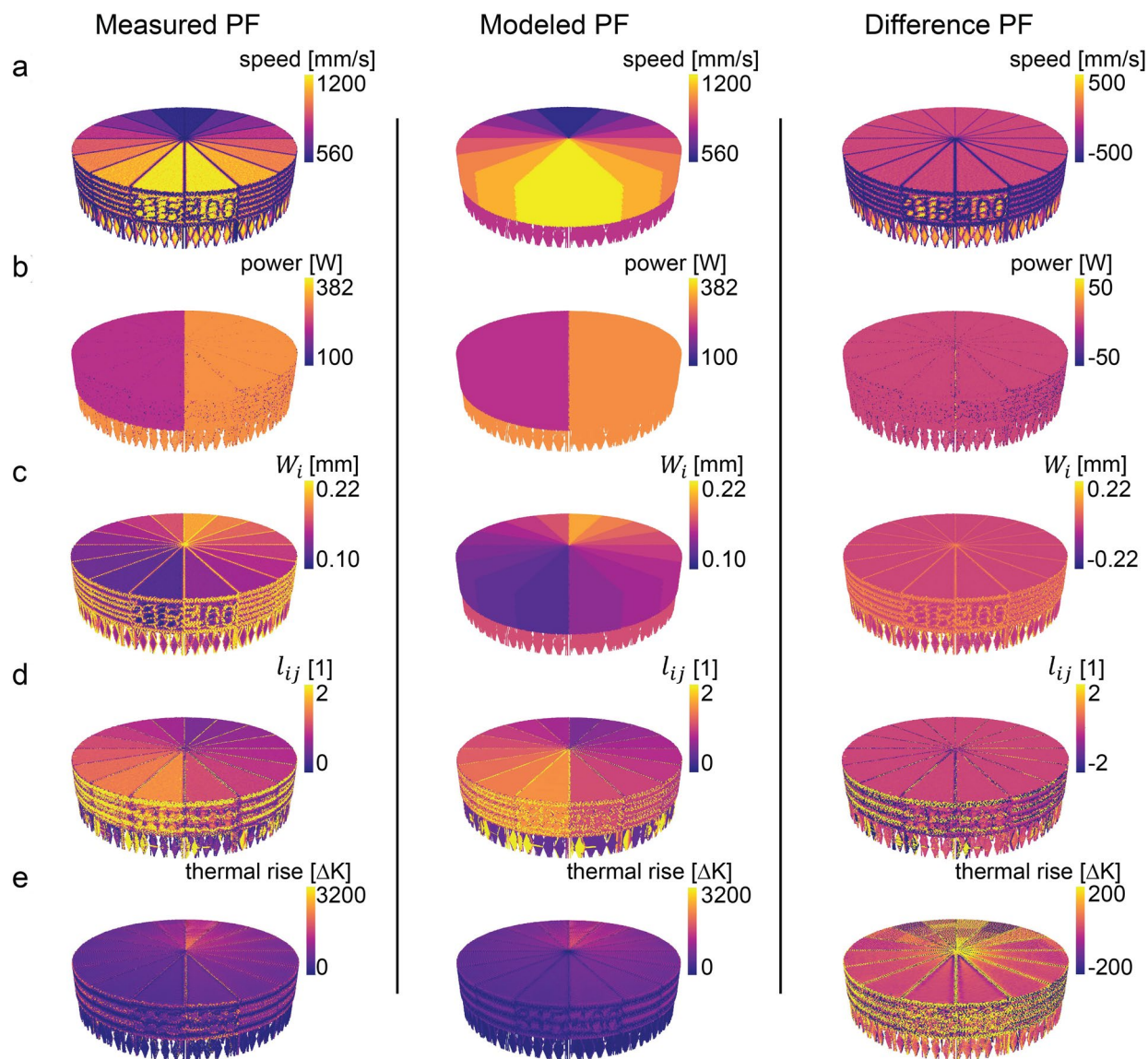


**Figure 6:** Measured, modeled and difference PF colormaps for the fields of (a) velocity, (b) power, (c) melt pool width, (d) lack of fusion, and (e) thermal rise.

fusion at the equiangular zone boundaries, Fig. 6(d), and thermal rise PMs throughout the test article, Fig. 6(e). A layer-wise thermal rise banding on the specimen outer wall was common to both the measured and modeled PFs, Fig. 6(e). For the measured PFs, a similar banding was also present on the speed, melt pool width, and lack of fusion PMs, while only the lack of fusion PM showed a similar banding for the modeled PF, Fig. 6(d). The modeled PFs were subtracted from the measured PFs to quantify the differences in the L-PBF AM processing and conduct direct comparisons between the expected and actual PMs.

The color scales used for the PM difference plots are restricted to increase the color contrast, Fig. 6. The mean, median, standard deviation, minimum, and maximum values for the PM

differences are reported as supplementary information, Table S1. The measured laser scan velocity at points along the equiangular zone boundaries showed high differences from the modeled velocity, and greater prevalence in the equiangular zones with higher velocities. However, within the equiangular zone interiors, the laser scan velocity difference was near zero with minimal difference values, Fig. 6(a). The melt pool width differences showed a similar trend as the velocity differences, Fig. 6(c). The differences in the power were prevalent at the interface between equiangular zones 1 and 9, Fig. 6(b). The lack of fusion PM differences with a magnitude greater than 2 were evenly distributed along the equiangular zone boundaries, Fig. 6(d). The thermal rise PM showed points of difference greater than 200  $\Delta K$  within

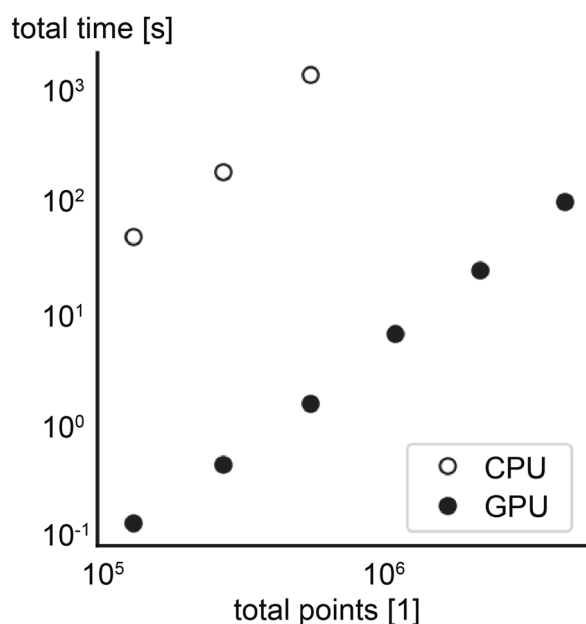


**Figure 7:** Comparison of the CPU only and the GPU accelerated computational time versus number of points in the PF.

equiangular zones 6–8 and 14–16. These were equiangular zones with lower velocities and higher thermal rise magnitudes. The thermal rise PM difference showed a negative trend towards the test article center and near the boundaries of the higher velocity equiangular zones 1 and 9, Fig. 6(e).

Modeled PFs with sizes ranging from 0.135 to 7.15 million points were evaluated using the AM-PM approach and the total time to compute was recorded. The performance of a central processing unit (CPU) bound computation was compared to a graphics processing unit (GPU) accelerated implementation. The CPU bound implementation encountered memory errors beyond 1 million points and required 900 times longer to compute the 0.58 million points than the GPU accelerated implementation, Fig. 7.

## Discussion

The Ti-6Al-4V cylindrical test article was designed to contain 16 equiangular zones built with different AM parameters, Table 1 and Fig. 2(a). These varied parameters and equiangular zone geometries combined to produce a wide range of L-PBF AM process conditions that were expected to result in lack of fusion porosity, fully consolidated material, and keyhole porosity. The measured and modeled PFs of this test article were used to explore the computational speed and utility of the AM-PM approach by quantifying correlations of melt track resolved process conditions to porosity.

The test article sub-geometries consisted of equiangular zones that transitioned from a wide area near the diameter to a

fine feature, point, towards the center. The point-wise process parameters of heat source intensity and velocity combined with the per equiangular zone geometry, sequence, slice, hatch patterns, layer wise hatch rotations, and instrument conditionals during the build to result in a wide range of melt track resolved process conditions. The variations in the surface features observed in the photograph of the specimen reflect this range of point-wise processing conditions per equiangular zone, between equiangular zones, and within equiangular zones, Fig. 2(b). Further details were observed using high resolution XCT.

The quality and accuracy of any analysis of correlations between PMs, point-wise processing conditions, and the porosity occurrence is dependent upon the quality and accuracy of the XCT segmentation, classification, and registration of porosity voxels to the points in the PF. If a porosity volume is below the detection limit of the XCT measurement, then it cannot be considered when conducting analysis of correlation between PM values and porosity occurrence. If the thresholding and classification methodology is either insensitive or hypersensitive, then the PM correlation analysis to porosity occurrence will be incomplete or misleading. If the registration quality of the XCT measurements to the PF is poor, then the PM correlation analysis to porosity occurrence will be poor. The utilization of the correlation analysis of PMs to porosity occurrence is a complex analysis that is bound to the uncertainty of the porosity measurement per point. The need remains for rigorous uncertainty propagation and quantification of this analysis.

Segmentation of grayscale images such as those derived from volumetric XCT inspections is a well-studied area of research that has produced a variety of methods from simple thresholding to approaches based on deep learning. However, the accuracy of porosity segmentation of XCT images of metallic AM components varies greatly across inspection systems and the choice of algorithm for segmentation [45]. Because the primary goal of this work is to introduce the PF driven PM approach, Otsu’s method [46, 47]<sup>1</sup> was applied to segment XCT images of the specimens since it requires no parameter tuning and can be parallelized across slices of the XCT-volume. The parallelization is also useful since the voxel intensity of XCT images of AM components is not uniform across the entire volume, and the relative dimensions of the background can vary from slice-to-slice. An important drawback to Otsu’s method is that it ignores the spatial information in each image. Subsequent work will analyze the dependence of the estimation of porosity on the choice of segmentation algorithm by comparing against

<sup>1</sup> Specific vendor and manufacturer names are explicitly mentioned only to accurately describe the software and hardware. The use of vendor and manufacturer names does not imply an endorsement by the U.S. Government nor does it imply that the specified equipment is the best available.



ground-truth estimates derived from optical microscope serial sectioning. This comparison will enable the analysis of specimens with more complex geometries.

The measured PF had irregular point positions and a layer-wise spacing of 50  $\mu\text{m}$ , whereas the nominal voxel size of the XCT was 12.7  $\mu\text{m}^3$ . The regular volumetric datatype and resolution of the XCT when registered with the PF positions allows for instances where porosity may be between layers and does not get registered into the PF. In this work, the XCT measured porosity had a 36  $\mu\text{m}$  equivalent diameter limit of detection and the registration was conducted on a precise coordinate basis to the measured PF. The point-wise registered porosity classification enabled correlation analysis of the porosity against the lack of fusion and thermal rise PMs such that trends were observed and may be used to inform statistical process controls.

The equiangular zone-wise populations are proportional to the equiangular zone-wise velocity parameter, higher in slower scanned equiangular zones, and lower in faster scanned equiangular zones. The correlation of total population with velocity is a direct result of the velocity being divided by the constant sampling rate of 12.5 kHz. The equiangular zones 1–3 were notably higher in porosity fraction, Fig. 3. Lack of fusion porosity was expected in those equiangular zones due to the smaller melt pool sizes that result from the higher velocity and lower power parameters.

The measured PF was used to compute the lack of fusion and thermal rise PMs throughout the build. The total population greatly outnumbered the porosity population, the total porosity point-wise population fraction was 0.01 for the specimen. Given that the total points significantly outnumber the porosity points, the PM heat maps for the specimen, Fig. 4(a) and Fig. 5(a), can be used to observe the overall PM trends across the different equiangular zones. The PM heat maps for the percent porosity population fraction, Fig. 4(b) and Fig. 5(b), can be used to determine correlations between the porosity and the PMs.

The Tang et al. [12] lack of fusion predictor model defines the lack of fusion threshold to be 1, as marked with the dashed line in Fig. 5. Most of the lack of fusion values for the porosity fraction was above the model threshold. Equiangular zones 1–3 had the greatest porosity population sizes, greater than 1 percent, Fig. 3. These equiangular zones had calculated melt pool widths, 117  $\mu\text{m}$  to 126  $\mu\text{m}$ , that were well correlated with the peak population lack of fusion value threshold, greater than 1, Fig. 5(b). There were also porosity fraction bins with lack of fusion values beneath the model threshold, values between 0.8 and 1. These binned values indicate point-wise process conditions where the Tang et al. [12] lack of fusion model does not explain the lack of fusion porosity existence. Spatter induced lack of fusion porosity occurs when the spatter welds to the surface and prevents complete fusion due to the increased surface material. Spatter with approximately 200  $\mu\text{m}$  height were

observed on the surface of the specimen by inspection of the XCT dataset. Spatter induced lack of fusion porosity can explain the peak porosity population points with a lack of fusion value less than 1. The porosity fraction showed a thermal rise threshold at 1000  $\Delta\text{K}$ , Fig. 4(b). It may follow that a PM thermal rise greater than 1000  $\Delta\text{K}$  was required to heal the spatter porosity during the AM process. Establishing the accuracy for each of the AM-PMs will be required.

The PF can be further used for process verification via deviation analysis when either a reference or a model PF is known, Fig. 6. The PF fields, both variables and PMs, can be visualized using 3D or layer-wise plots to diagnose if the process variables have been prescribed correctly in build files, or if the build performed as expected via PM analysis. For the test article, it was observed that the measured PF velocity and power had deviations from their modeled values at the interfaces between equiangular zones, Fig. 6(a, b). The interfaces between equiangular zones are the turnaround regions, where hatch lines start and stop. The deviations for velocity were widest in the equiangular zones with greater assigned velocity. The prominent deviations in velocity at greater velocities is related to the kinetics of the moving mirrors attached to the IntelliSCAN<sup>®</sup> galvanometers. The moving mirrors have momenta proportional to the changing velocities and their respective mass. Momentum effects are known and often addressed with advanced velocity and power synchronization tactics [48–51]. During the turnaround at high velocities, the position and power values require greater tolerance due to the mirror momentum and power-position timing of the IntelliSCAN<sup>®</sup> galvanometers, or advanced instrument tuning [52, 53]. The power deviations appeared to have the greatest prominence between the two fastest regions, where each was set at a different power value. The deviation plot of the calculated melt pool widths, Fig. 6(c), appeared to have deviations that reflected the trend observed in the velocity deviation plot, Fig. 6(a). The lack of fusion deviation plot, Fig. 6(d), also showed a similar trend as the velocity deviation plot, Fig. 6(a). The thermal rise deviation plot, Fig. 6(e), showed prominent deviations at the interfaces between the highest velocity equiangular zones 1 and 9, Fig. 6(a), with additional deviations in the slower regions, equiangular zones 7, 8, 15, and 16. The momentum of the mirrors is the primary cause for the equiangular zone interface deviations. Layer-wise banding was observed on the outer wall of the cylinder for the speed, melt pool width, lack of fusion, and thermal rise AM-PMs for the measured PF, and for the modeled PF, lack of fusion and thermal rise. The layer-wise banding was the result of layer-wise hatch sequence and rotations. The lack of fusion spikes at the turn around regions in the modeled PF were an artifact of the neighborhood search algorithm and indicate an opportunity for an improved neighborhood search algorithm. The thermal rise PM difference showed a negative trend towards the test article center and

near the boundaries of the higher velocity equiangular zones 1 and 9, Fig. 6(e). This negative trend indicated that the thermal rise PM of the measured PF, from the actual build, was cooler than expected by the modeled PF, based on the build file. This trend was due to a laser-galvanometer mirror synchronization delay setting that was poorly tuned for those mirror velocities. These insights into the L-PBF AM process were enabled by the PF driven AM-PM approach through deviation analysis, e.g., a fingerprint style build-to-build statistical process control framework.

The AM-PM approach was coded using Python libraries for both CPU and GPU accelerated implementations. The test article took 4 h to build, and 6.5 min to compute the PMs from the measured 5.8-million-point PF. A thermal finite element modeling (FEM) approach is understood to be capable of superior accuracy in process temperature predictions over the thermal analytical calculations that are required for an AM-PM approach. Yavari et al. [39] reported ~12 h to compute a 1-million-node finite element-based thermal modeling approach that when extrapolated for a 5.8-million-node computation the cost becomes ~3 days. The comparable finite element-based thermal modeling approach has an estimated computational cost that is ~665 times greater than the AM-PM approach. The largest computational cost for an AM-PM calculation is the neighborhood search. AM-PM calculations were restricted to analytical process models and a single time step such that the PMs were calculated using a single pass through the PF for maximal compute speed. The 900× faster GPU acceleration over the CPU bound calculation demonstrated the PF driven AM-PM approach is fully parallel, Fig. 7. The parallel and scalable calculation design and the direct comparison of build file generated modeled PFs against in-situ monitoring PFs are advantages of the PF and PM approach to AM modeling and assessment. The computational speed of the AM-PM approach enables iterative assessment and tuning of AM builds using the point-wise PM metrics, Fig. 8.

## Summary

AM-PM calculations described in this work have a maximal computational speed for quantifying melt track resolved process conditions from PF data. The PMs for the 5.8-million-point measured PF of the test article were calculated in 6.5 min, ~665× faster than a similarly sized thermal FEM calculation. The GPU accelerated AM-PM calculation enables efficient prediction, assessment, and adjustment of AM builds for reducing defects and developing statistical process controls.

The elegance of the AM-PM approach is in the allowance for multiple analytical AM models to be calculated directly from a PF in a single pass and requires only material property inputs. A PF can be either modeled from a build file or measured from

in-situ sensors. Both measured and modeled PFs were demonstrated for the test article. The differences between the PMs that were calculated from the measured and modeled PFs were quantified and trends that offered insight into the process were discussed. The momentum of the galvanometer mirrors was identified as having a tremendous influence over the differences between the measured and modeled PF driven velocity PMs.

The PF data and the calculated AM-PMs in this work are single time step, point-in-time, data that were spatially mapped to XCT measured porosity existence within the test article. The porosity of the test article was measured using XCT with Otsu's thresholding. The test article was designed to promote a range of localized process conditions that were conducive to either keyhole or lack of fusion formation mechanisms of porosity, but only lack of fusion porosity was apparent in the XCT measured porosity data. Porosity fraction bins with lack of fusion PMs between 0.8 and 1 were observed, which indicated that additional physics are needed to describe the lack of fusion porosity existence.

## Methodology

### Computational

The AM-PM approach was demonstrated using Python libraries. The PyCUDA module [54] was used for GPU accelerated calculations. A CPU based computation that used the Numba [55], NumPy [56], and SciPy [57] compute modules was also developed. The workstation used for a computational comparison was a ×64-based PC with a dual socket Intel Xeon® E5-2667v4™ on a Supermicro® SYS-7038A-i™, with 128 Gb of RAM, and an Nvidia® Titan V™ GPU.

### Point field

A model PF was generated using the common layer interface type build file instructions, along with the L-PBF AM instrument settings. The generated points were spaced by the velocity divided by the sampling frequency for each build step. A sampling frequency of 12.5 kHz was used. The power was assigned per point according to the power of each build step. Instrument conditionals were used for the generation of the timestamps for the modeled PF. Two delays were used: (1) a layer-wise spreading delay of 140 s and (2) a mirror settling delay of 50 μs. The mirror settling delay occurs at each toggle of the laser heat source.

The measured PF is the second approach specified in the PM process chart, Fig. 8. A measured PF is an in situ process record of the galvanometer position synchronized with laser power readings per unit time. The laser focus was kept constant with a gaussian spot size of 80 μm diameter.

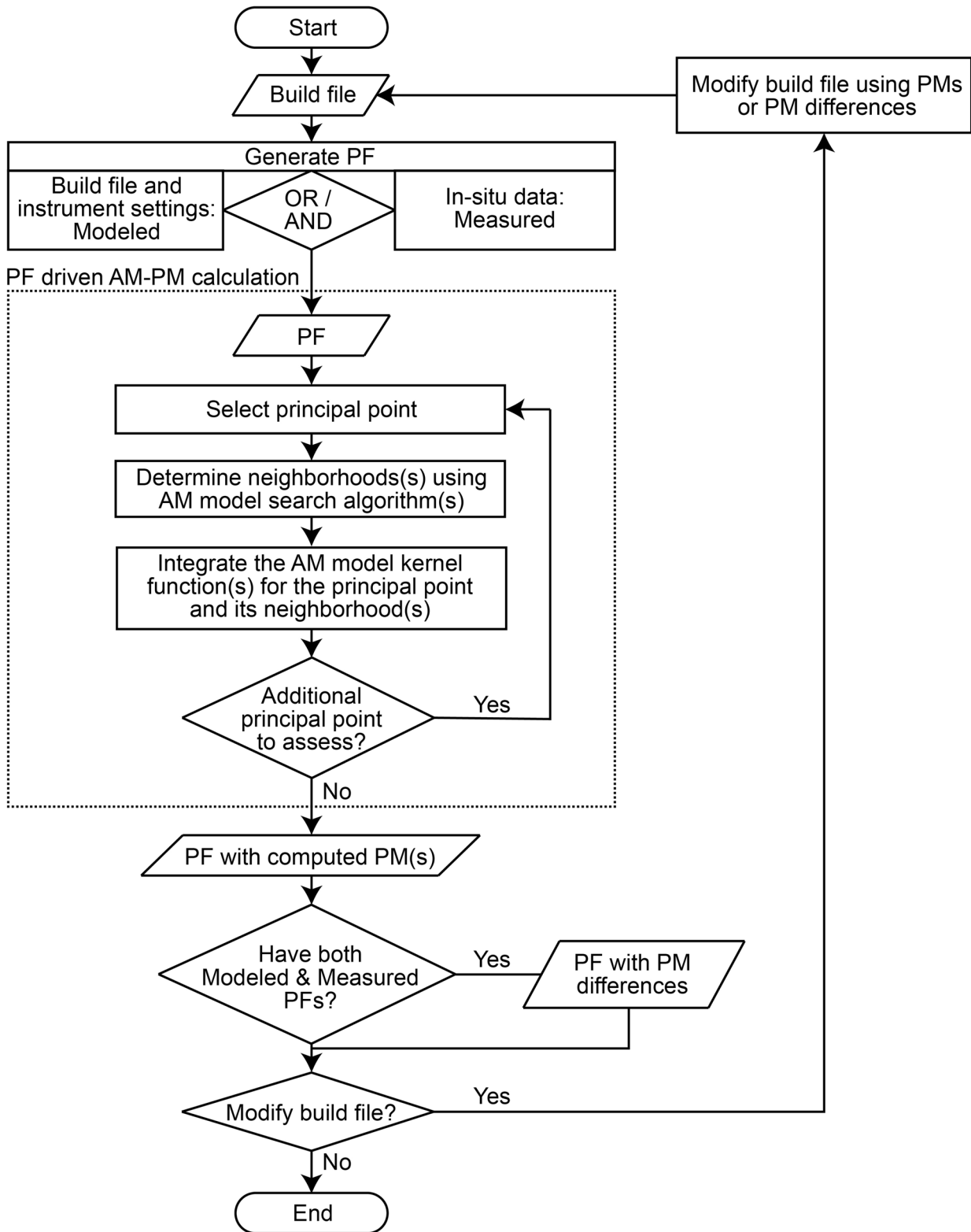


Figure 8: Sequence diagram of the PF driven AM-PM calculation.

## Experimental

A configurable additive testbed (CAT) was used for building and recording the measured PF. The term configurable implies that both hardware and software can be re-designed to facilitate experiments that support additive manufacturing research and development. The CAT was configured with an environmental chamber such that the build was done with  $< 10$  ppm  $O_2$ , measured using a PureAire® trace oxygen analyzer. A SCANLAB® GmbH IntelliScan® III 20 galvanometer head was driven by a SCANLAB® RTC6™ control board and an IPG Photonics® modulated continuous emission 1070 nm laser with a maximum power of 1 kW to conduct the build steps, fusing the feedstock in the L-PBF AM manner. The feedstock was a titanium alloy Ti-6Al-4V atomized spherical powder,  $53 \pm 15 \mu\text{m}$ , sourced from ATT®. A Jenoptik® F-Theta lens with a 255 mm working distance was used for a near uniform laser spot diameter of  $80 \mu\text{m}$  across the build area.

For each point in the measured PF, the x-location was measured from the first galvanometer mirror return, the y-location was measured from the second galvanometer mirror return, time was metered by the RTC6 real time clock control board, and power was measured from the IPG Photonics® laser analog output using a LabJack™ T7 Pro™ and a 25 kHz sampling rate. The power measurements were synchronized with the location and time via triggers from the RTC6™ control board.

## Test article

A test article was built. The test article was a cylinder with a 21 mm diameter, a 3.2 mm height, and 16 equiangular zones, Fig. 3 and Table 1. A hatch spacing of 0.100 mm, inter-layer rotation angle of 0.297 radians and an inter-layer height of  $50 \mu\text{m}$  were used. The specimen was built at room temperature and atop a 2 mm tall support structure, for a total build height of 5.2 mm. The starting hatch angle, the hatch angle at the 2.05 mm layer height, was varied for each equiangular zone so that the hatch angles would have equivalent hatch patterns relative to each equiangular zone. The starting angles,  $\theta_H^{2.05}$ , are listed per equiangular zone in Table 1.

The thermophysical properties of Ti-6Al-4V were estimated based on reported values at 150 °C: thermal conductivity was  $8.1 \text{ W}\cdot\text{m}^{-1}\text{ K}^{-1}$  [58], density was  $4400 \text{ kg}\cdot\text{m}^{-3}$  [59], and specific heat capacity was  $630 \text{ J}\cdot\text{kg}^{-1}\text{ K}^{-1}$  [60].

The PM calculations were carried out on both the modeled and measured PFs. The modeled and measured PFs have different coordinates and values. The modeled PF was mapped to the nearest neighbor measured PF. The differences between the measured and modeled fields were determined by subtracting the model from the measured field values.

## Characterization

Post-fabrication imaging of the test article was executed using a Nikon® Metrology HMXST 225™ X-ray system. The system can resolve details down to  $5 \mu\text{m}$ . System settings during data acquisition and volumetric reconstruction were a voltage of 190 kV, a current intensity of  $57 \mu\text{A}$ , a focal spot size of  $5 \mu\text{m}$ , a rotational step angle of 0.002 radians, and a reconstructed voxel resolution of  $12.8 \mu\text{m}$  from 3142 projections. A previous study [32] of porosity in AM Ti-6Al-4V components demonstrated that these XCT settings are suitable to detect voids of equivalent spherical diameter greater than  $38 \mu\text{m}$ , 3 voxel-lengths in the XCT reconstruction.

A standard segmentation method due to Otsu [46] provides an estimate of the porosity in the specimens. The Otsu threshold binary classification of porosity and bulk phases was thereby registered to the PF locations as a measure of porosity or bulk per point.

## Registration

Registration of the XCT voxels to the PF was done by manual determination of 6 spatial coordinates from the PF that correspond to 6 voxel coordinates from the XCT. The least-squares optimal mapping was computed from these 6 correspondences of XCT to PF coordinates. In other words, the affine mapping  $f(x) = Ax + b$  from PF to XCT coordinates was defined to minimize the sum of residuals, i.e.  $f = \operatorname{argmin}_{\{A,b\}} \left\{ \sum_{i=1}^6 |Ax_i + b - y_i|^2 \right\}$ , where  $x_i$  and  $y_i$  are the identified PF and XCT landmark points, and  $A \in R^{3 \times 3}$  and  $b \in R^3$ .

## Acknowledgments

The authors gratefully acknowledge the National Aeronautics and Space Administration (NASA) Aeronautics Research Mission Directorate's (ARMD) Transformational Tools and Technologies (TTT) project for supporting this work; the Advanced Materials and Processing branch, and the Nondestructive Evaluation Sciences branch at NASA Langley Research Center for laboratory and facility support. The authors would also like to thank William P. Sommer for collecting the XCT data and discussions on XCT reconstruction; Dr. Erik L. Frankforter for discussions leading to the registration and segmentation of the XCT data. SJAH would like to acknowledge Prof. Anthony D. Rollett and Prof. Thomas O'Connor for a helpful discussion regarding visualization and terminology; Dr. Lopamudra Das for helpful discussions regarding readability; Peter L. Messick, Joel A. Alexa, and James B. Thornton for operational assistance on the CAT; and Harold D. Claytor for build preparation and specimen imaging.

## Author contributions

SJAH: Conceptualization, Methodology, Software, Formal Analysis, Investigation, Resources, Data curation, Writing—Original Draft, Writing—Review & Editing, Visualization, Project Administration. BR: Conceptualization, Formal Analysis, Methodology, Writing—Review & Editing, Visualization. PWS: Methodology, Formal Analysis, Writing—Review & Editing. ARK: Writing—Review & Editing. JNZ: Writing—Review & Editing. EHG: Writing—Review & Editing, Supervision, Funding acquisition.

## Funding

This work was funded by the NASA TTT project in ARMD.

## Data availability

The data and code that support the findings of this study are available from NASA but restrictions apply to the availability of these data, which were used under license for the current study, and so are not publicly available. Data and code are however available from the corresponding author upon reasonable request and with permission of NASA.

## Declarations

**Conflict of interest** The authors declare that they have no conflict of interest.

## Open Access

This article is licensed under a Creative Commons Attribution 4.0 International License, which permits use, sharing, adaptation, distribution and reproduction in any medium or format, as long as you give appropriate credit to the original author(s) and the source, provide a link to the Creative Commons licence, and indicate if changes were made. The images or other third party material in this article are included in the article's Creative Commons licence, unless indicated otherwise in a credit line to the material. If material is not included in the article's Creative Commons licence and your intended use is not permitted by statutory regulation or exceeds the permitted use, you will need to obtain permission directly from the copyright holder. To view a copy of this licence, visit <http://creativecommons.org/licenses/by/4.0/>.

## Supplementary Information

The online version contains supplementary material available at <https://doi.org/10.1557/s43578-023-00953-7>.

## References

1. B. Blakey-Milner, P. Gradl, G. Snedden, M. Brooks, J. Pitot, E. Lopez, M. Leary, F. Berto, A. du Plessis, Metal additive manufacturing in aerospace: a review. *Mater. Des.* **209**, 110008 (2021)
2. R. Russell, D. Wells, J. Waller, B. Poorganji, E. Ott, T. Nakagawa, H. Sandoval, N. Shamsaei, M. Seifi, Qualification and certification of metal additive manufactured hardware for aerospace applications. *Add Manuf Aerosp Indus* (2019). <https://doi.org/10.1016/B978-0-12-814062-8.00003-0>
3. I. Yadroitsev, I. Yadroitsava, A. Du Plessis, E. MacDonald, *Fundamentals of laser powder bed fusion of metals* (Elsevier, Amsterdam, 2021)
4. Y. Zhang, L. Wu, X. Guo, S. Kane, Y. Deng, Y.-G. Jung, J.-H. Lee, J. Zhang, Additive manufacturing of metallic materials: a review. *J. Mater. Eng. Perform.* **27**(1), 1–13 (2018)
5. Anik, Y., 2021, *Additive Manufacturing—General Principles—Fundamentals and Vocabulary*, 52900:2021, ISO/ASTM.
6. Gradl, P. R., Greene, S. E., Protz, C., Bullard, B., Buzzell, J., Garcia, C., Wood, J., Osborne, R., Hulka, J., and Cooper, K. G., 2018, "Additive Manufacturing of Liquid Rocket Engine Combustion Devices: A Summary of Process Developments and Hot-Fire Testing Results," *2018 Joint Propulsion Conference*, American Institute of Aeronautics and Astronautics, Cincinnati, Ohio.
7. T.D. Ngo, A. Kashani, G. Imbalzano, K.T.Q. Nguyen, D. Hui, Additive manufacturing (3D Printing): a review of materials, methods, applications and challenges. *Compos. Part B Eng.* **143**, 172–196 (2018)
8. S. Kim, S.K. Moon, A part consolidation design method for additive manufacturing based on product disassembly complexity. *Appl. Sci.* **10**(3), 1100 (2020)
9. S. Mohd Yusuf, S. Cutler, N. Gao, Review: the impact of metal additive manufacturing on the aerospace industry. *Metals* **9**(12), 1286 (2019)
10. W.H. Kan, M. Gao, X. Zhang, E. Liang, N.S.L. Chiu, C.V.S. Lim, A. Huang, The influence of porosity on Ti-6Al-4V parts fabricated by laser powder bed fusion in the pursuit of process efficiency. *Int. J. Adv. Manuf. Technol.* **119**(7–8), 5417–5438 (2022)
11. Luna, S., 2021, *Additive Manufacturing Requirements for Space-flight Systems*, NASA-STD-6030, National Aeronautics and Space Administration, Houston, TX.
12. M. Tang, P.C. Pistorius, J.L. Beuth, Prediction of lack-of-fusion porosity for powder bed fusion. *Addit. Manuf.* **14**, 39–48 (2017)
13. P. Zagade, B.P. Gautham, A. De, T. DebRoy, Analytical estimation of fusion zone dimensions and cooling rates in part scale laser powder bed fusion. *Addit. Manuf.* **46**, 102222 (2021)
14. J.V. Gordon, S.P. Narra, R.W. Cunningham, H. Liu, H. Chen, R.M. Suter, J.L. Beuth, A.D. Rollett, Defect structure process maps for laser powder bed fusion additive manufacturing. *Addit. Manuf.* **36**, 101552 (2020)
15. A.A. Martin, N.P. Calta, S.A. Khairallah, J. Wang, P.J. Depond, A.Y. Fong, V. Thampy, G.M. Guss, A.M. Kiss, K.H. Stone, C.J.

- Tassone, J.N. Weker, M.F. Toney, T. van Buuren, M.J. Matthews, Dynamics of pore formation during laser powder bed fusion additive manufacturing. *Nat. Commun.* **10**(1), 1987 (2019)
16. D. Rosenthal, Mathematical theory of heat distribution during welding and cutting. *Weld J* **20**(5), 220–234 (1941)
  17. Y. Yang, A. Großmann, P. Kühn, J. Mölloney, L. Kropholler, C. Mittelstedt, B.-X. Xu, Validated dimensionless scaling law for melt pool width in laser powder bed fusion. *J. Mater. Process. Technol.* **299**, 117316 (2022)
  18. A. Thanki, L. Goossens, A.P. Ompusunggu, M. Bayat, A. Bey-Temsamani, B. Van Hooreweder, J.-P. Kruth, A. Witvrouw, Melt pool feature analysis using a high-speed coaxial monitoring system for laser powder bed fusion of Ti-6Al-4V grade 23. *Int. J. Adv. Manuf. Technol.* **120**(9–10), 6497–6514 (2022)
  19. A. Gaikwad, R.J. Williams, H. de Winton, B.D. Bevans, Z. Smoqi, P. Rao, P.A. Hooper, Multi phenomena melt pool sensor data fusion for enhanced process monitoring of laser powder bed fusion additive manufacturing. *Mater. Des.* **221**, 110919 (2022)
  20. Yeratapally, S. R., Lang, C., and Glaessgen, E. H., 2020, “A Computational Study to Investigate the Effect of Defect Geometries on the Fatigue Crack Driving Forces in Powder-Bed AM Materials,” *AIAA Scitech 2020 Forum*, American Institute of Aeronautics and Astronautics, Orlando, FL.
  21. S.R. Yeratapally, C.G. Lang, A.R. Cerrone, G.L. Niebur, K. Cronberger, Effect of defects on the constant-amplitude fatigue behavior of as-built Ti-6Al-4V alloy produced by laser powder bed fusion process: assessing performance with metallographic analysis and micromechanical simulations. *Addit. Manuf.* **52**, 102639 (2022)
  22. W. Wang, J. Ning, S.Y. Liang, Analytical prediction of keyhole porosity in laser powder bed fusion. *Int. J. Adv. Manuf. Technol.* **119**(11–12), 6995–7002 (2022)
  23. N.H. Paulson, B. Gould, S.J. Wolff, M. Stan, A.C. Greco, Correlations between thermal history and keyhole porosity in laser powder bed fusion. *Addit. Manuf.* **34**, 101213 (2020)
  24. M. Bayat, A. Thanki, S. Mohanty, A. Witvrouw, S. Yang, J. Thorborg, N.S. Tiedje, J.H. Hattel, Keyhole-induced porosities in Laser-Based Powder Bed Fusion (L-PBF) of Ti6Al4V: high-fidelity modelling and experimental validation. *Addit. Manuf.* **30**, 100835 (2019)
  25. A. Mostafaei, C. Zhao, Y. He, S. Reza Ghiaasiaan, B. Shi, S. Shao, N. Shamsaei, Z. Wu, N. Kouraytem, T. Sun, J. Pauza, J.V. Gordon, B. Webler, N.D. Parab, M. Asherloo, Q. Guo, L. Chen, A.D. Rollett, Defects and anomalies in powder bed fusion metal additive manufacturing. *Curr. Opin. Solid State Mater. Sci.* **26**(2), 100974 (2022)
  26. B. AlMangour, D. Grzesiak, T. Borkar, J.-M. Yang, Densification behavior, microstructural evolution, and mechanical properties of TiC/316L stainless steel nanocomposites fabricated by selective laser melting. *Mater. Des.* **138**, 119–128 (2018)
  27. Cowles, B., 2016, “Summary Report: Joint Federal Aviation Administration, Air Force Workshop on Qualification,” Certif. Addit. Manuf. Parts.
  28. Edward H. Glaessgen, Lyle E. Levine, Paul W. Witherell, Donmez, M. A., Gorelik, M., Ashmore, N. A., Barto, R. R., Battaile, C. C., Millwater, H. R., Nanni, G. J., Rollett, A. D., Schwalbach, E. J., and Venkatesh, V., 2021, *NASA/NIST/FAA Technical Interchange Meeting on Computational Materials Approaches for Qualification by Analysis for Aerospace Applications*, NASA/TM-20210015175, National Aeronautics and Space Administration, Hampton, VA
  29. S.A. Khairallah, A.T. Anderson, A. Rubenchik, W.E. King, Laser powder-bed fusion additive manufacturing: physics of complex melt flow and formation mechanisms of pores, spatter, and denudation zones. *Acta Mater.* **108**, 36–45 (2016)
  30. S.T. Strayer, W.J.F. Templeton, F.X. Dugast, S.P. Narra, A.C. To, Accelerating high-fidelity thermal process simulation of laser powder bed fusion via the Computational Fluid Dynamics Imposed Finite Element Method (CIFEM). *Addit. Manuf. Lett.* **3**, 100081 (2022)
  31. A.J. Pinkerton, L. Li, Modelling the geometry of a moving laser melt pool and deposition track via energy and mass balances. *J. Phys. Appl. Phys.* **37**(14), 1885–1895 (2004)
  32. M.A. Groeber, E. Schwalbach, S. Donegan, K. Chaput, T. Butler, J. Miller, Application of characterization, modelling, and analytics towards understanding process-structure linkages in metallic 3D printing. *IOP Conf. Ser. Mater. Sci. Eng.* **219**, 012002 (2017)
  33. E.J. Schwalbach, S.P. Donegan, M.G. Chapman, K.J. Chaput, M.A. Groeber, A discrete source model of powder bed fusion additive manufacturing thermal history. *Addit. Manuf.* **25**, 485–498 (2019)
  34. A.J. Wolfer, J. Aires, K. Wheeler, J.-P. Delplanque, A. Rubenchik, A. Anderson, S. Khairallah, Fast solution strategy for transient heat conduction for arbitrary scan paths in additive manufacturing. *Addit. Manuf.* **30**, 100898 (2019)
  35. B. Stump, A. Plotkowski, An adaptive integration scheme for heat conduction in additive manufacturing. *Appl. Math. Model.* **75**, 787–805 (2019)
  36. Z. Yang, Y. Lu, H. Yeung, S. Krishnamurty, From scan strategy to melt pool prediction: a neighboring-effect modeling method. *J. Comput. Inf. Sci. Eng.* **20**(5), 051001 (2020)
  37. F. Fruggiero, A. Lambiase, R. Bonito, M. Fera, The load of sustainability for additive manufacturing processes. *Procedia Manuf.* **41**, 375–382 (2019)
  38. Yavari, R., Severson, J., Gaikwad, A., Cole, K., and Rao, P., 2019, “Predicting part-level thermal history in metal additive manufacturing using graph theory: experimental validation with directed energy deposition of titanium alloy parts,” *Volume 1: additive manufacturing manufacturing equipment and systems bio and sustainable manufacturing*, American Society of Mechanical Engineers

39. Yavari, R., Cole, K. D., and Rao, P., 2019, "A graph theoretic approach for near real-time prediction of part-level thermal history in metal additive manufacturing processes," *Volume 1: additive manufacturing manufacturing equipment and systems bio and sustainable manufacturing*, American Society of Mechanical Engineers
40. K.D. Cole, M.R. Yavari, P.K. Rao, Computational heat transfer with spectral graph theory: quantitative verification. *Int. J. Therm. Sci.* **153**, 106383 (2020)
41. M.R. Yavari, R.J. Williams, K.D. Cole, P.A. Hooper, P. Rao, Thermal modeling in metal additive manufacturing using graph theory: experimental validation with laser powder bed fusion using in situ infrared thermography data. *J. Manuf. Sci. Eng.* **142**(12), 121005 (2020)
42. Rao, P. K., Kong, Z., Duty, C. E., and Smith, R. J., 2016, "Three Dimensional Point Cloud Measurement Based Dimensional Integrity Assessment for Additive Manufactured Parts Using Spectral Graph Theory," *Volume 2: Materials: Biomanufacturing: Properties, Applications and Systems: Sustainable Manufacturing*, American Society of Mechanical Engineers.
43. R. Yavari, Z. Smoqi, A. Riensche, B. Bevans, H. Kobir, H. Mendoza, H. Song, K. Cole, P. Rao, Part-scale thermal simulation of laser powder bed fusion using graph theory: effect of thermal history on porosity, microstructure evolution, and recoater crash. *Mater. Des.* **204**, 109685 (2021)
44. G. Tapia, S. Khairallah, M. Matthews, W.E. King, A. Elwany, Gaussian process-based surrogate modeling framework for process planning in laser powder-bed fusion additive manufacturing of 316L stainless steel. *Int. J. Adv. Manuf. Technol.* **94**(9–12), 3591–3603 (2017)
45. B.R. Jolley, M.D. Uchic, D. Sparkman, M. Chapman, E.J. Schwalbach, Application of serial sectioning to evaluate the performance of X-ray computed tomography for quantitative porosity measurements in additively manufactured metals. *JOM* **73**(11), 3230–3239 (2021)
46. N. Otsu, A threshold selection method from gray-level histograms. *IEEE Trans. Syst. Man Cybern.* **9**(1), 62–66 (1979)
47. S. van der Walt, J.L. Schönberger, J. Nunez-Iglesias, F. Boulogne, J.D. Warner, N. Yager, E. Gouillart, T. Yu, Scikit-image: image processing in python. *PeerJ* **2**, e453 (2014)
48. Jaeggi, B., Neuenschwander, B., Zimmermann, M., Zecherle, M., and Boeckler, E. W., 2016, "Time-Optimized Laser Micro Machining by Using a New High Dynamic and High Precision Galvo Scanner," B. Neuenschwander, S. Roth, C.P. Grigoropoulos, and T. Makimura, eds., San Francisco, California, United States, p. 973513.
49. M. Pothen, K. Winands, F. Klocke, Compensation of scanner based inertia for laser structuring processes. *J. Laser Appl.* **29**(1), 012017 (2017)
50. Sabo, D. A., Brunner, D., and Engelmayer, A., 2005, "Advantages of Digital Servo Amplifiers for Control of a Galvanometer Based Optical Scanning System," San Diego, California, USA, p. 113
51. H. Yeung, B.M. Lane, M.A. Donmez, J.C. Fox, J. Neira, Implementation of advanced laser control strategies for powder bed fusion systems. *Procedia Manuf.* **26**, 871–879 (2018)
52. F. Rasoanarivo, D. Dumur, P. Rodriguez-Ayerbe, "Improving SLM additive manufacturing operation precision with H-infinity controller structure", *CIRP. J. Manuf. Sci. Technol.* **33**, 82–90 (2021)
53. A. Koglbauer, S. Wolf, O. Marten, K. Reinhard, Investigation on laser scanner synchronization via advanced beam path analysis in 3D additive manufacturing systems. *J. Laser MicroNanoengineering* **13**(2), 140 (2018)
54. A. Klöckner, N. Pinto, Y. Lee, B. Catanzaro, P. Ivanov, A. Fasih, PyCUDA and PyOpenCL: a scripting-based approach to GPU run-time code generation. *Parallel Comput.* **38**(3), 157–174 (2012)
55. Lam, S. K., Pitrou, A., and Seibert, S., 2015, "Numba: A LLVM-Based Python JIT Compiler," *Proceedings of the Second Workshop on the LLVM Compiler Infrastructure in HPC-LLVM '15*, ACM Press, Austin, Texas, pp. 1–6.
56. C.R. Harris, K.J. Millman, S.J. van der Walt, R. Gommers, P. Virtanen, D. Cournapeau, E. Wieser, J. Taylor, S. Berg, N.J. Smith, R. Kern, M. Picus, S. Hoyer, M.H. van Kerkwijk, M. Brett, A. Haldane, J.F. del Río, M. Wiebe, P. Peterson, P. Gérard-Marchant, K. Sheppard, T. Reddy, W. Weckesser, H. Abbasi, C. Gohlke, T.E. Oliphant, Array programming with NumPy. *Nature* **585**(7825), 357–362 (2020)
57. P. Virtanen, R. Gommers, T.E. Oliphant, M. Haberland, T. Reddy, D. Cournapeau, E. Burovski, P. Peterson, W. Weckesser, J. Bright, S.J. van der Walt, M. Brett, J. Wilson, K.J. Millman, N. Mayorov, A.R.J. Nelson, E. Jones, R. Kern, E. Larson, C.J. Carey, Í. Polat, Y. Feng, E.W. Moore, J. VanderPlas, D. Laxalde, J. Perktold, R. Cimrman, I. Henriksen, E.A. Quintero, C.R. Harris, A.M. Archibald, A.H. Ribeiro, F. Pedregosa, P. van Mulbregt, SciPy 1.0 Contributors, A. Vijaykumar, A.P. Bardelli, A. Rothberg, A. Hilboll, A. Kloeckner, A. Scopatz, A. Lee, A. Rokem, C.N. Woods, C. Fulton, C. Masson, C. Häggström, C. Fitzgerald, D.A. Nicholson, D.R. Hagen, D.V. Pasechnik, E. Olivetti, E. Martin, E. Wieser, F. Silva, F. Lenders, F. Wilhelm, G. Young, G.A. Price, G.-L. Ingold, G.E. Allen, G.R. Lee, H. Audren, I. Probst, J.P. Dietrich, J. Silterra, J.T. Webber, J. Slavič, J. Nothman, J. Buchner, J. Kulick, J.L. Schönberger, J.V. de Miranda Cardoso, J. Reimer, J. Harrington, J.L.C. Rodríguez, J. Nunez-Iglesias, J. Kuczynski, K. Tritz, M. Thoma, M. Newville, M. Kümmerer, M. Bolingbroke, M. Tartre, M. Pak, N.J. Smith, N. Nowaczyk, N. Shebanov, O. Pavlyk, P.A. Brodtkorb, P. Lee, R.T. McGibbon, R. Feldbauer, S. Lewis, S. Tygier, S. Sievert, S. Vigna, S. Peterson, S. More, T. Pudlik, T. Oshima, T.J. Pingel, T.P. Robitaille, T. Spura, T.R. Jones, T. Cera, T. Leslie, T. Zito, T. Krauss, U. Upadhyay, Y.O. Halchenko, Y. Vázquez-Baeza, SciPy 1.0: fundamental algorithms for scientific computing in python. *Nat. Methods* **17**(3), 261–272 (2020)
58. K. Bartsch, D. Herzog, B. Bossen, C. Emmelmann, Material modeling of Ti–6Al–4V alloy processed by laser powder bed

- fusion for application in macro-scale process simulation. Mater. Sci. Eng. A **814**, 141237 (2021)
59. K.C. Mills, *Ti-6Al-4V (IMI 318), Recommended values of thermophysical properties for selected commercial alloys* (Elsevier, Amsterdam, 2002), pp.211–217
60. D. Basak, R.A. Overfelt, D. Wang, Measurement of specific heat capacity and electrical resistivity of industrial alloys using pulse heating techniques. Int. J. Thermophys. **24**(6), 1721–1733 (2003)

**Publisher's Note** Springer Nature remains neutral with regard to jurisdictional claims in published maps and institutional affiliations.